THE ROYAL SOCIETY

Published online 30 September 2002

Simulations of the ^{1}H electron spin echo–electron nuclear double resonance and ^{2}H electron spin echo envelope modulation spectra of exchangeable hydrogen nuclei coupled to the S_2-state photosystem II manganese cluster

Constantino P. Aznar and R. David Britt*

Department of Chemistry, University of California, Davis, 1 Shields Avenue, Davis, CA 95616, USA

The pulsed EPR methods of electron spin echo envelope modulation (ESEEM) and electron spin echo–electron nuclear double resonance (ESE–ENDOR) are used to investigate the proximity of exchangeable hydrogens around the paramagnetic S_2-state Mn cluster of the photosystem II oxygen-evolving complex. Although ESEEM and ESE–ENDOR are both pulsed electron paramagnetic resonance techniques, the specific mechanisms by which nuclear spin transitions are observed are quite different. We are able to generate good simulations of both ^{1}H ESE–ENDOR and ^{2}H ESEEM signatures of exchangeable hydrogens at the S_2-state cluster. The convergence of simulation parameters for both methods provides a high degree of confidence in the simulations. Several exchangeable protons–deuterons with strong dipolar couplings are observed. In the simulations, two of the close (≈2.5 Å) hydrogen nuclei exhibit strong isotropic couplings and are therefore most probably associated with direct substrate ligation to paramagnetic Mn. Another two of the close (≈2.7 Å) hydrogen nuclei show no isotropic couplings and are therefore most probably not contained in Mn ligands. We suggest that these proximal hydrogens may be associated with a Ca^{2+}-bound substrate, as indicated in recent mechanistic proposals for O_2 formation.

Keywords: multiline electron paramagnetic resonance signal; oxygen-evolving complex; pulsed electron paramagnetic resonance; water oxidation

1. INTRODUCTION

PS II oxygen evolution occurs through a cycle of five 'S-state' intermediates, S_0 through to S_4, where the subscript represents the number of oxidizing equivalents abstracted from the PS II OEC by the photoxidized P_{680}^+ Chl moiety (Kok *et al.* 1970). The OEC consists of a tetranuclear Mn cluster, the redox-active tyrosine Y_Z and the essential cofactors Cl^- and Ca^+ (Debus 1992; Britt 1996; Yachandra *et al.* 1996). Extensive CW EPR characterization of the odd-electron S_2 state has led to much of our current knowledge of the structure, protein ligation, and substrate and inhibitor binding modes of the Mn cluster. However, CW EPR spectroscopy has inherent resolution limitations that can often be overcome by performing pulsed EPR experiments using multipulse ESE sequences. In this article, we discuss results from our laboratory using ESEEM and ESE–ENDOR to address the proximity of exchangeable hydrogen nuclei (protons and deuterons) to the Mn cluster in the S_2 state. The goal of this work is to learn more about the binding of substrate water within the OEC at the S_2 state, which is halfway through the S_2-state water oxidation cycle.

* Author for correspondence (rdbritt@ucdavis.edu).

One contribution of 21 to a Discussion Meeting Issue 'Photosystem II: molecular structure and function'.

2. PULSED EPR METHODS

These ESE methods are useful because EPR lineshapes of biological paramagnetic entities are typically dominated by inhomogeneous broadening. The inhomogeneously broadened lineshape arises from the overlap of resonances ('spin packets') resulting from a near continuum of magnetic environments. One source of inhomogeneous broadening is the unresolved overlap of hyperfine lines from many coupled nuclei, because the number of hyperfine lines increases multiplicatively with the number of classes of coupled nuclei. If the spectral density becomes sufficiently high, the spacing between individual hyperfine lines will become less than the intrinsic lifetime-broadened linewidth of each spin packet, and the EPR lineshape will become dominated by the resulting Gaussian lineshape, such as in the case of the $g = 4.1$ signal in unoriented PSII membranes (Casey & Sauer 1984; Zimmermann & Rutherford 1984). Even for a partially resolved signal such as the S_2-state multiline (Dismukes & Siderer 1981), much spectral information is buried by the inhomogeneous broadening: only 18–21 peaks are resolved out of the 1296 transitions resulting from four $I = 5/2$ ^{55}Mn couplings. In addition to unresolved hyperfine, inhomogeneous broad-

DOI 10.1098/rstb.2002.1144

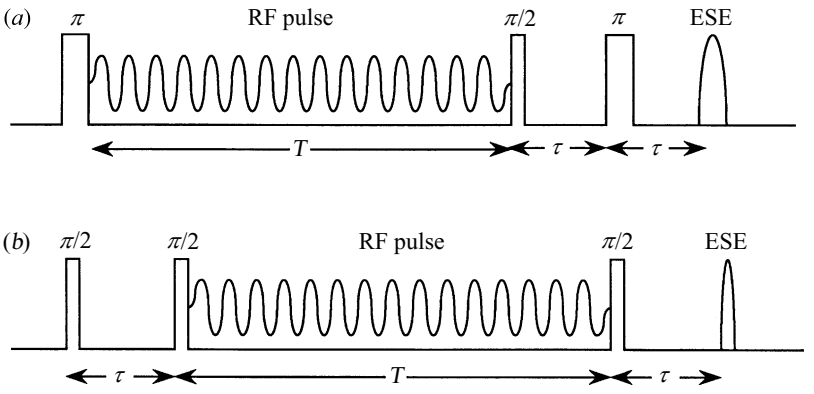

Figure 1. (*a*) Two-pulse and (*b*) three-pulse ESEEM sequences.

ening results from orientational distribution of anisotropic hyperfine and *g*-matrix interactions as well as site-to-site 'strain' of *g* and *A* terms.

Spin echo sequences, either two pulse or three pulse, can be used to negate the effects of inhomogeneous broading. The resultant spin echo signal can be used to generate a field swept EPR spectrum analogous to the conventional CW EPR spectrum. Field modulation is not employed, so the spectrum generated is a measure of the direct absorption rather than the field derivative. More importantly, by overcoming the deleterious effects of inhomogeneous broadening obscuring hyperfine interactions with magnetic nuclei, ESE methods can introduce much new spectral information. Specifically, the ESEEM and ESE–ENDOR techniques can be used to detect the nuclear spin transitions of magnetic nuclei in close proximity to the paramagnetic centre (Hoffman *et al.* 1993; Britt *et al.* 2000). In these experiments the spin echo is the carrier onto which nuclear spin information is encoded, either by time-domain interference (ESEEM) or through RF-driven magnetization transfer (ESE–ENDOR).

(a) *ESEEM*

In the ESEEM experiment, ESEs are formed by the application of two or more resonant microwave pulses. In addition to inducing the electron spin transitions, the microwave pulses may also induce 'semi-forbidden' transitions of nuclear spins magnetically coupled to the electron spins, resulting in quantum mechanical coherences in the nuclear spin sublevels associated with the electron spin levels. These coherences create interference effects that can be measured by varying the ESE pulse timing. Fourier analysis of the resulting time-domain ESEEM pattern reveals the frequencies of the nuclear spin transitions. The frequencies and amplitudes of the Fourier peaks can be interpreted to determine hyperfine and electric quadrupolar interactions of the coupled nuclei. Time-domain simulations may also be used to determine the number of coupled nuclei of a given class. This *quantitative* aspect is a major advantage offered by the ESEEM technique. In general, ESEEM excels for relatively weakly coupled nuclei. ESEEM experiments utilizing two-pulse Hahn echo (figure 1*a*) or three-pulse 'stimulated' echo (figure 1*b*) sequences have been applied to the study of the PSII Mn cluster. In this paper, we target deuterons introduced into the vicinity of the S_2-state Mn cluster by PSII membrane incubation in a ^2H_2O-enriched buffer.

(b) *ESE–ENDOR*

Unlike ESEEM, the ESE–ENDOR experiments do not rely on semi-forbidden nuclear spin transitions during the microwave pulses. Rather, the nuclear transitions are driven directly with separate high-power RF pulses. In an ESE–ENDOR experiment, an alteration of the initial electron spin magnetization is created by one or more high-power resonant microwave pulses. Application of the RF pulse further perturbs the electron magnetization if the RF pulse induces spin transitions of nuclei magnetically coupled to the electron spins. The nuclear spin transition frequencies are measured by varying the RF while monitoring the effect of the RF pulse on a subsequent ESE. The ESE–ENDOR sequences are capable of detecting nuclei that are too strongly coupled for ESEEM detection. Therefore ESE–ENDOR is a more robust method. Alternatively, ESE–ENDOR can also be used to target ESEEM-active nuclei as well. Pulse sequences introduced by Davies (1974) and by Mims (1965) have been applied to the PSII Mn cluster (figure 2). The Davies sequence is typically preferable for large couplings, while the Mims sequence provides ESE–ENDOR access to relatively weak couplings. In this paper, we use Davies ESE–ENDOR to examine the distribution of protons around the S_2-state Mn cluster. A comparison of the ^1H ESE–ENDOR spectrum taken before and after PSII membranes are incubated in a ^2H_2O-enriched buffer allows us to focus on the same exchangeable hydrogen sites observed with the ^2H ESEEM. The constraints provided by simulating both ^1H ESEEM and ^2H ESE–ENDOR using the identical sets of hyperfine coupling parameters, scaled appropriately for the relative gyromagnetic ratios ($\gamma(^1H)/\gamma(^2H) = 6.5$), provide for appreciably greater confidence in the results than if only one of the techniques was employed.

(c) *ESEEM and ESE–ENDOR spectral trends*

Figure 3 illustrates ^1H ESE–ENDOR patterns through simulations of 'powder pattern' spectra for a single nuclear spin $I = 1/2$ proton coupled to a spin $I = 1/2$ electron. These simulations are generated in the limit of a point dipole approximation. In a first-order perturbation theory analysis, the ENDOR transitions come in pairs, centred at the proton Larmor frequency, and split by the hyperfine coupling A, which is angularly dependent because of the dipolar coupling. The dipolar coupling term has a magnitude

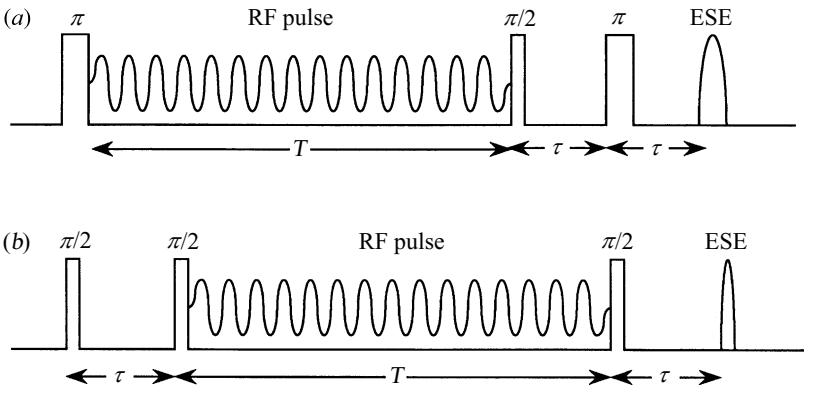

Figure 2. (*a*) The Davies and (*b*) the Mims ESE–ENDOR sequences.

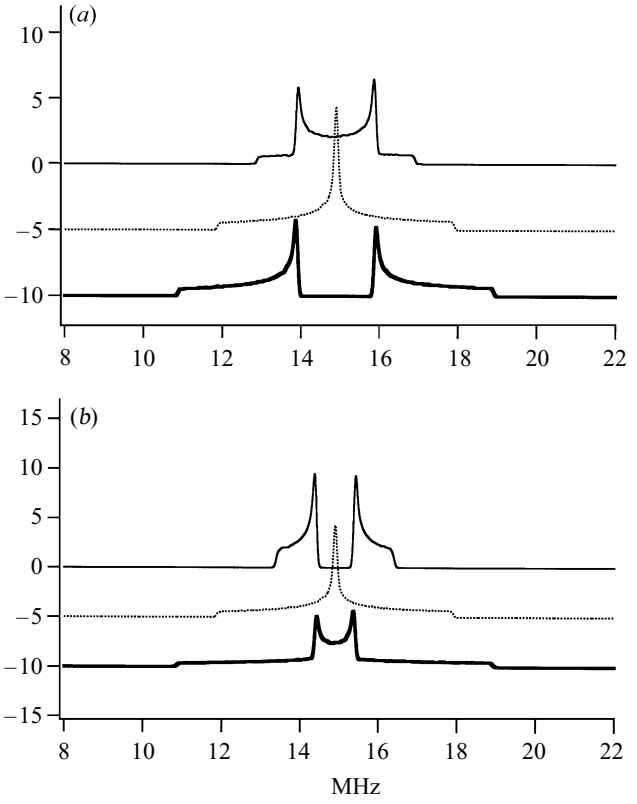

Figure 3. ^{1}H ESE–ENDOR simulations. (*a*) The A_{iso} dependence for fixed A_{dip}, where $A_{dip} = 2.00$ MHz and $r_{eff} = 3.41$ Å: solid line, $A_{iso} = 0.00$ MHz; dotted line, $A_{iso} = 2.00$ MHz; bold solid line, $A_{iso} = 4.00$ MHz. (*b*) The A_{dip} dependence for fixed A_{iso}, where $A_{iso} = 2.00$ MHz: solid line, $A_{dip} = 1.00$ MHz, $r_{eff} = 4.91$ Å; dotted line, $A_{dip} = 2.00$ MHz, $r_{eff} = 3.41$ Å; bold solid line, $A_{dip} = 3.00$ MHz, $r_{eff} = 2.97$ Å.

$$A_{dip} = \frac{g_e \beta_e g_N \beta_N}{hr^3},$$

where g_e and g_N are the electron and proton *g* factors and β_e and β_N are the electron and proton magnetons. In this term, *r* is the ESE–ENDOR separation, again in the point dipolar approximation. The dipolar interaction follows a $3\cos^2\theta - 1$ angular dependence, where θ is the angle between the ESE–ENDOR vector and the applied magnetic field vector. There can also be an isotropic hyperfine component, A_{iso}, which arises from the direct overlap of the unpaired electron wavefunction with the magnetic proton. For a given orientation, the effective hyperfine coupling is given by $A_{iso} + A_{dip}(3\cos\theta - 1)$. In this point dipole approximation, the powder patterns show axial symmetry, with greatest intensity at the 'perpendicular' turning point which results in the limit where the ESE–ENDOR vector approaches an orientation perpendicular to the applied magnetic field vector ($\theta \rightarrow 90°$). The 'parallel' turning point has less intensity because a smaller fraction of the unit sphere corresponds to orientations with the ESE–ENDOR vector nearly parallel to the applied magnetic field vector ($\theta \rightarrow 90°$).

Figure 3 shows ^{1}H ENDOR simulations for the case where A_{dip} and A_{iso} have the same sign. Figure 3*a* shows the A_{iso} dependence for fixed A_{dip}, and figure 3*b* shows the A_{dip} dependence for fixed A_{iso}. For a relatively large A_{iso} (figure 3*a*, bottom trace) the two powder patterns are separated. If A_{dip} and A_{iso} have the same sign, the convention utilized here, the perpendicular features are the innermost, with the smaller parallel features outermost. As A_{iso} is decreased (middle trace) the two powder patterns coalesce, initially overlapping the perpendicular features, and as A_{iso} approaches zero (top trace), the two powder patterns completely overlap. Figure 3*b* shows analogous effects as A_{dip} is increased, from top to bottom, for a fixed value of A_{iso}.

Of course in the 'real world' the powder patterns are not typically so well resolved. For example, hyperfine strain will reduce the sharpness of the perpendicular and parallel turning points compared with the ideal simulation. Often the smaller parallel transitions are difficult to detect, as could be imagined for the large A_{dip} case at the bottom of figure 3*c*. Additionally, if the actual unpaired electron density distribution is non-spherical, the powder patterns will generally take on some degree of rhombicity. In cases with well defined *g*-anisotropy, at a given field value the full powder pattern will not be obtained because only certain molecular orientations are actually sampled (Hoffman *et al.* 1993). However, for ESE–ENDOR of the S_2-state multiline EPR signal obtained at X-band EPR frequencies, such *g*-anisotropy is negligible and full powder pattern simulations are appropriate.

Figure 4 shows the ^{2}H two-pulse ESEEM patterns, both in the time and frequency domain, corresponding to the ESE–ENDOR spectra of figure 3. The hyperfine terms, A_{iso} and A_{dip}, are all divided by the $\gamma(^1H)/\gamma(^2H) = 6.5$ ratio

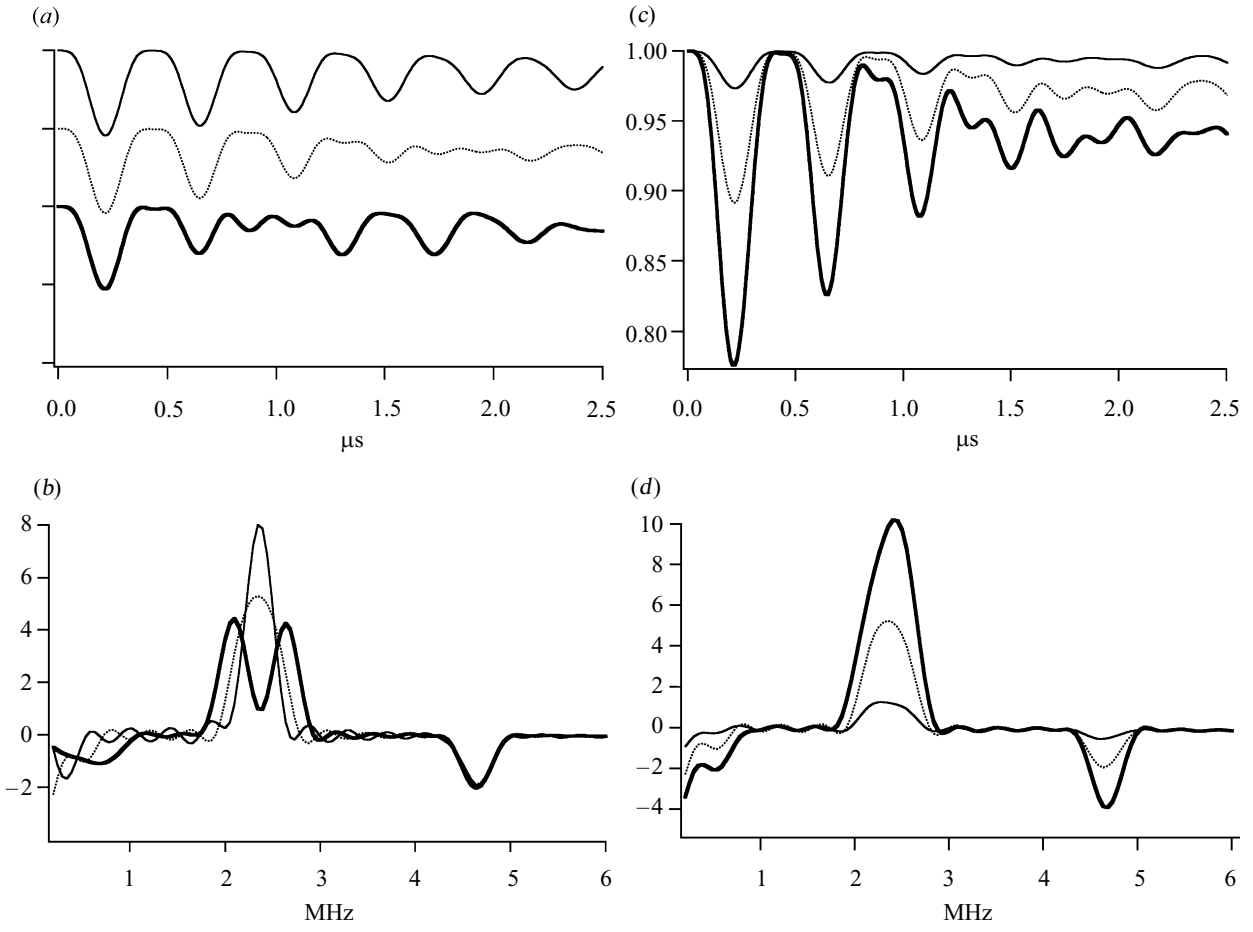

Figure 4. ^{2}H ESEEM simulations. (*a*,*c*) Time-domain spectra. (*b*,*d*) Frequency-domain spectra. (*a*,*b*) The A_{iso} dependence for fixed A_{dip}, where $A_{dip} = 0.31$ MHz and $r_{eff} = 3.41$ Å: solid line, $A_{iso} = 0.00$ MHz; dotted line, $A_{iso} = 0.31$ MHz; bold solid line, $A_{iso} = 0.61$ MHz. (*c*,*d*) The A_{dip} dependence for fixed A_{iso}, where $A_{iso} = 0.31$ MHz: solid line, $A_{dip} = 0.15$ MHz, $r_{eff} = 4.91$ Å; dotted line, $A_{dip} = 0.31$ MHz, $r_{eff} = 3.41$ Å; bold solid line, $A_{dip} = 0.46$ MHz, $r_{eff} = 2.97$ Å.

for these simulations, and electric quadrupolar parameters of $e^2qQ = 0.22$ MHz and $\eta = 0.1$ are used for simulations for this nuclear spin $I = 1$ nucleus. The simulations are carried out via a matrix diagonalization program previously described (Britt *et al.* 1989) based on the density matrix calculations described by Mims (1972). Figure 4*a*,*b* shows the data for fixed A_{dip} and varied A_{iso} values. The modulation depths in the time-domain spectra do not change too dramatically with varied A_{iso}, and are shown staggered in figure 4*a*. However, the overall modulation details do show a large dependence on the hyperfine parameters, and thus the simulation of time-domain signatures can be used to extract hyperfine couplings from experimental data. The frequency-domain spectra were obtained by Fourier transformation. The fundamental transitions are centred at the ^{2}H Larmor frequency, ν_N. One notes that the resolution is poor compared with the ESE–ENDOR spectra. This is in large part due to the fact that in the point dipolar limit, the semi-allowed nuclear spin transitions necessary for the modulation effect become fully forbidden at the canonical $\theta = 0$, 90° turning points. Thus, one gets zero intensity at the very frequencies that are emphasized in the ENDOR spectrum. For the A_{iso} dependent data of figure 4*a*,*b*, in the frequency domain one only sees a broad featureless peak for the two lower A_{iso} values. For the largest A_{iso} simulation, the peak does split into a doublet.

A negative feature is also observed at approximately twice the ^{2}H Larmor frequency. This 180° out-of-phase feature occurs at the sum of the frequencies of the two fundamental transitions. The exact frequency of this transition is useful because it is shifted from twice ν_N by a factor of

$$\frac{9}{16}(A_{dip})^2,\nu_N.$$

Thus, the position of this peak gives specific information concerning the dipolar coupling. This out-of-phase sum peak is narrower than the fundamental, and thus progressively manifests itself in the time domain. For example, in the middle traces of figure 4*a*,*b*, note how the almost sinusoidal modulation at the fundamental frequency slowly turns into a second harmonic component. Simulating such transitions helps extract the isotropic and dipolar couplings from the experimental data. Kevan (1979) gives a very good description of such effects.

Figure 4*c*,*d* shows the dramatic effects of varying A_{dip} for a fixed A_{iso}. The modulation depth increases dramatically with increased dipolar coupling. In terms of distance, the modulation depth scales as *ca.* $1/r^6$. The time-domain

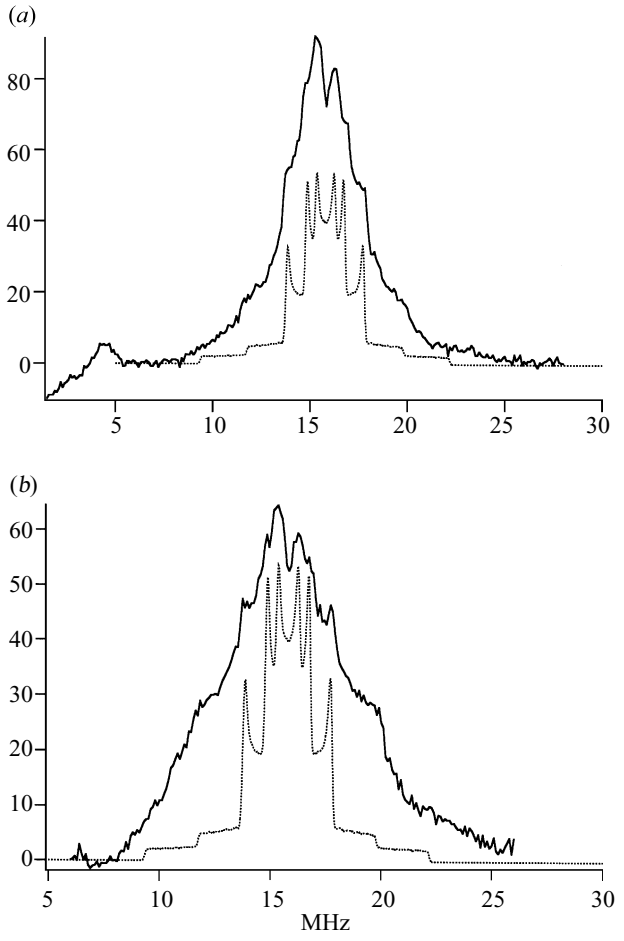

Figure 5. ^{1}H ESE–ENDOR of the S_2-state multiline signal. (*a*) Data obtained with 100 ns $\pi/2$ pulses. (*b*) Data obtained with 50 ns $\pi/2$ pulses. The solid lines represent experimental data. The dotted lines display the simulation using the ^{1}H parameters of table 1.

data of figure 4*c*,*d* are all plotted with the same amplitude at the initial $\tau = 0$ point. Note in the frequency domain that both the fundamental and the out-of-phase harmonic peaks increase dramatically in amplitude with increasing A_{dip} values. The modulation amplitude damps out more quickly as A_{dip} increases, which is reflected in the wider Fourier transforms. Also, one can observe the frequency shifting of the harmonic peak with increased A_{dip} as described above.

3. SIMULATIONS OF S_2-STATE ESEEM AND ESE–ENDOR SPECTRA

As discussed in § 1, we have used both ^{1}H ESE–ENDOR and ^{2}H ESEEM to examine the proximity of exchangeable hydrogens in the immediate vicinity of the Mn cluster. 'BBY' PSII-enriched spinach membranes (Berthold *et al.* 1981) were used. Pulsed EPR experiments were performed both before illumination (background) and after 200 K illumination to generate the S_2 state. Preparation and sample treatment details are provided in Gilchrist (1996) and will be published elsewhere. The focus of this paper is on the simultaneous simulation of datasets obtained with the two complementary pulsed EPR methods.

Table 1. Simulation parameters.

number	A_{iso} (MHz) ^{2}H (^{1}H)	A_{dip} (MHz) ^{2}H (^{1}H)	r_{eff} (Å)
2	0.55 (3.58)	0.70 (4.56)	2.59
1	0.00 (0.00)	0.61 (3.97)	2.71
1	0.00 (0.00)	0.30 (1.95)	3.43
ambient waters	0.00 (0.00)	$\leqslant$ 0.19 ($\leqslant$ 1.24)	$\geqslant$ 4.00

Figure 5 shows the ^{1}H ESE–ENDOR spectrum associated with the S_2-state multiline EPR signal. Figure 5*a* shows data obtained with 100 ns $\pi/2$ microwave pulses. Figure 5*b* shows data obtained with 50 ns $\pi/2$ microwave pulses, which accentuates the strongest coupled ENDOR features. Background spectra obtained before illumination (not shown) exhibit none of the structured ^{1}H ESE–ENDOR features. These are produced upon illumination, and can thus be associated with the S_2 state. Additionally, these all disappear following 60 min ^2H_2O incubation (data not shown). The same ^2H_2O incubation gives rise to deep ^{2}H modulations in two- and three-pulse ESEEM experiments (figure 6*a*,*b*). The time-domain traces displayed are derived from light–dark subtracted datasets for both deuterated and natural abundance buffers. The normalized deuterated dataset is point-by-point divided by the natural abundance dataset to generate a 'ratioed' time-domain spectrum emphasizing the effects of the ^2H_2O exchange. Frequency-domain spectra (figure 6*c*,*d*) are obtained via Fourier transformation.

Given these complementary datasets, the challenge is to simulate these with identical sets of hyperfine matrices. We have done this quite successfully. The dotted lines in figure 5 show a ^{1}H ESE–ENDOR simulation using three classes of coupled protons. This same set of coupled hydrogen nuclei gives excellent two- and three-pulse (figure 6, dotted lines) ^{2}H ESEEM simulations. Simulation parameters are provided in table 1. The dipolar couplings are reported both in frequency units and in terms of effective point-dipolar distances. The first column reports the number of nuclei in the class. This number originates from the quantitative aspect of ESEEM simulation. The ESEEM simulation also employs a number of 'ambient' distant ($\approx$4 Å) deuterons which contribute to the ^{2}H modulation. These ^{2}H ESEEM simulations are able to reproduce the very deep modulation and the rapid modulation damping for both the two- and three-pulse cases. In the two-pulse ESEEM simulation, the proper amplitude and phasing of the out-of-phase harmonic term is also reproduced well. This term does not contribute to the three-pulse ESEEM patterns.

4. DISCUSSION

The combination of ^{1}H ESE–ENDOR and ^{2}H ESEEM allows us to describe several classes of exchangeable hydrogens in close proximity to the S_2-state Mn cluster. In a point dipole approximation, the closest of these hydrogen nuclei are at distances on the order of 2.6–2.7 Å, which would be consistent with water or hydroxide ligation to Mn. We are working on using multipoint dipole modelling (Force *et al.* 1998), with distributed spin den-

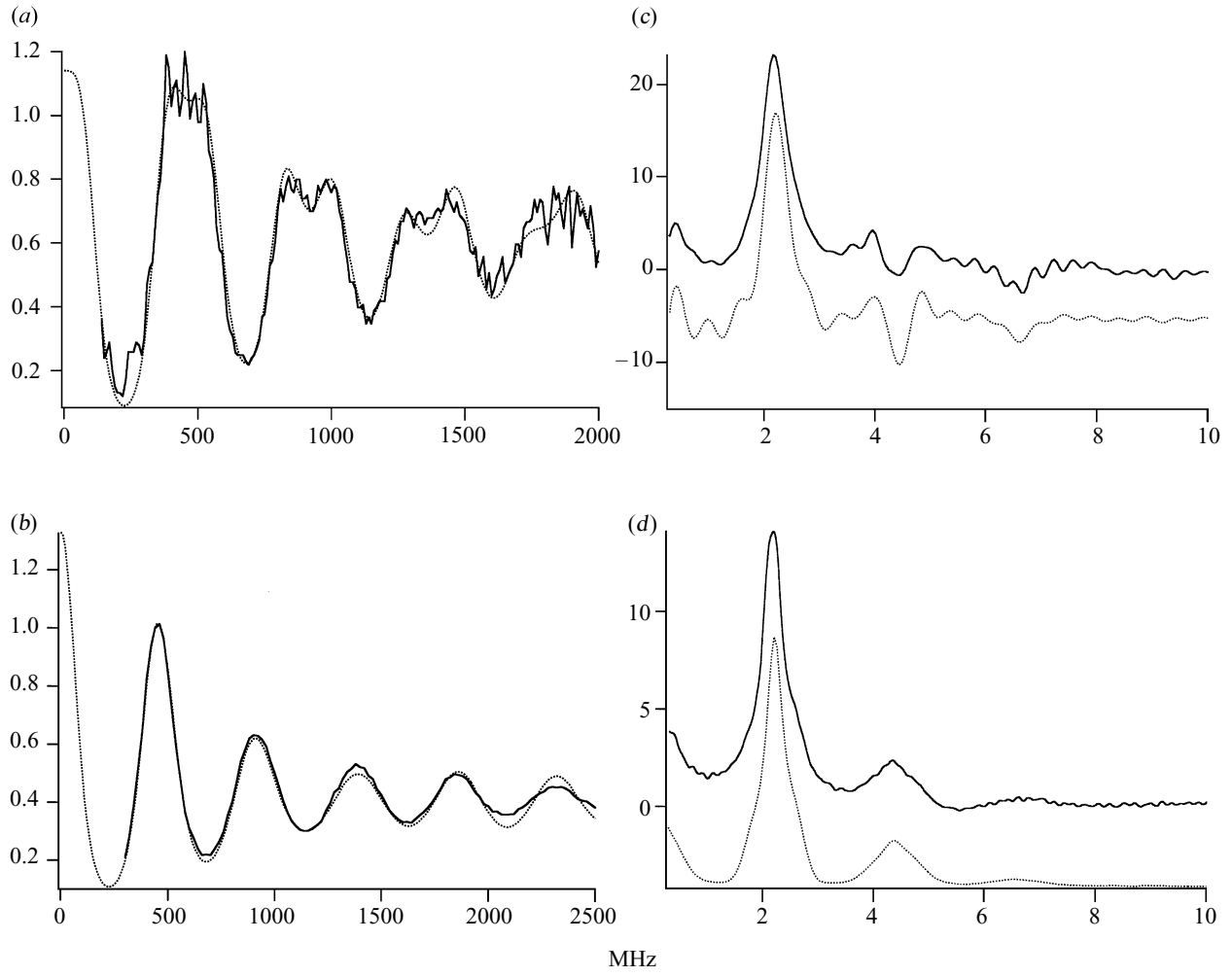

Figure 6. (*a*,*b*) ^2H (*a*) two-pulse and (*b*) three-pulse ESEEM of the S_2-state multiline signal. Solid lines display the experimental time-domain data resulting from ratioing light–dark datasets for deuterated and proteated buffer samples. The dotted lines show simulations using the ^2H parameters of table 1. (*c*,*d*) Data and simulations from the frequency domain with (*c*) two-pulse and (*d*) three-pulse ESEEM. Solid lines display the experimental data and dotted lines the stimulated data.

sities on structural model for the Mn cluster as determined by our ^{55}Mn ENDOR experiments (Peloquin *et al.* 2000), to more rigorously model the distances probed by the dipolar couplings. However, we tentatively assign these short-distance exchangeable hydrogens to water(s) or hydroxide(s) bound at the Mn cluster of the OEC. The strong hyperfine interactions that give rise to these assignments were not observed in previous continuous wave ENDOR experiments (Kawamori *et al.* 1989; Tang *et al.* 1993; Fiege *et al.* 1996), probably because of the large breadth of the resultant ENDOR powder patterns. These data and their simulations together support a model of a 'wet' environment for the S_2-state Mn cluster, with substrate water derived ligands already bound by S_2.

One interesting substrate water binding possibility arises from an examination of the hyperfine couplings in table 1. The class described in the first row, with the largest dipolar coupling and the shortest dipolar distance (2.59 Å), also has an appreciable isotropic hyperfine coupling (3.58 MHz), which is consistent with it corresponding to a direct ligand to a paramagnetic Mn ion (Randall *et al.* 1997). However, the class described in the second row, with a 2.71 Å dipolar distance, is simulated with only a dipolar coupling. It is not obvious how water or hydroxide ligand bound directly to a paramagnetic Mn ion could have zero isotropic hyperfine coupling. However, recent mechanistic models for O–O bond formation have utilized the required Ca^{2+} cofactor as the metal binding site for the second substrate water (Pecoraro *et al.* 1998; Limburg *et al.* 1999; Vrettos *et al.* 2001). Perhaps such a structural geometry gives rise to hydrogens positioned close to the Mn cluster but with very small isotropic coupling.

We acknowledge the National Institutes of Health (GM48242) for support of this research. Pulsed EPR data were provided by M. L. Gilchrist, D. W. Randall, D. A. Force, J. A. Ball and J. M. Peloquin.

REFERENCES

Berthold, D. A., Babcock, G. T. & Yocum, C. F. 1981 A highly resolved, oxygen-evolving photosystem II preparation from spinach thylakoid membranes. *FEBS Lett.* **134**, 231–234.

Britt, R. D. 1996 Oxygen evolution. In *Oxygenic photosynthesis: the light reactions* (ed. D. Ort & C. F. Yocum), pp. 137–164. Dordrecht, The Netherlands: Kluwer.

Britt, R. D., Zimmermann, J.-L., Sauer, K. & Klein, M. P. 1989 Ammonia binds to the catalytic manganese of the oxy-

gen-evolving complex of photosystem II. Evidence by electron spin-echo envelope modulation spectroscopy. *J. Am. Chem. Soc.* **111**, 3522–3532.
Britt, R. D., Peloquin, J. M. & Campbell, K. A. 2000 Pulsed and parallel polarization EPR characterization of the manganese cluster of the photosystem II oxygen evolving complex. *A. Rev. Biophys. Biomol. Struct.* **29**, 463–495.
Casey, J. L. & Sauer, K. 1984 EPR dectection of a cryogenically photogenerated intermediate in photosynthetic oxygen evolution. *Biochim. Biophys. Acta* **767**, 21–28.
Davies, E. R. 1974 A new pulse ENDOR technique. *Phys. Lett.* A **47**, 1–2.
Debus, R. J. 1992 The manganese and calcium ions of photosynthetic oxygen evolution. *Biochim. Biophys. Acta* **1102**, 269–352.
Dismukes, G. C. & Siderer, Y. 1981 Intermediates of a polynuclear manganese center involved in photosynthetic oxidation of water. *Proc. Natl Acad. Sci. USA* **78**, 274–278.
Fiege, R., Zweygart, W., Bittl, R., Adir, N., Genger, G. & Lubitz, W. 1996 EPR and ENDOR studies of the water oxidizing complex of photosystem II. *Photosyn. Res.* **48**, 227–237.
Force, D. A., Randall, D. W., Lorigan, G. A., Clemens, K. L. & Britt, R. D. 1998 ESEEM studies of alcohol bindingto the manganese cluster of the oxygen evolving complex of photosystem II. *J. Am. Chem. Soc.* **120**, 13 321–13 333.
Gilchrist, M. L. 1996 Pulsed electron paramagnetic resonance investigations of photosynthetic oxygen evolution. PhD dissertation, University of California, Davis, CA, USA.
Hoffman, B. M., DeRose, V. J., Doan, P. E., Gurbiel, R. J., Houseman, A. L. P. & Telser, J. 1993 Metalloenzyme active-site structure and function through multifrequency cw and pulsed ENDOR. In *Biological magnetic resonance*, vol. 13 (ed. L. J. Berliner & J. Reuben), pp. 151–218. New York: Plenum.
Kawamori, A., Inui, T., Ono, T. & Inoue, Y. 1989 ENDOR study on the position of hydrogens close to the manganese cluster in S2 state of photosystem-II. *FEBS Lett.* **254**, 151–154.
Kevan, L. 1979 Modulation of electron spin-echo decay in solids. In *Time domain electron spin resonance* (ed. L. Kevan & R. N. Schwartz), pp. 279–341. New York: Wiley.
Kok, B., Forbush, B. & McGloin, M. 1970 Coorperation of charges in photosynthetic O_2 evolution. I. A linear four step mechanism. *Photochem. Photobiol.* **11**, 457–475.
Limburg, J., Szalai, V. A. & Brudvig, G. W. 1999 A mechanistic and structural model for the formation and reactivity of a Mn–V=O species in photosynthetic water oxidation. *J. Chem. Soc. Dalton Trans.* **1999**, 1353–1361.
Mims, W. B. 1965 Pulsed ENDOR experiments. *Proc. R. Soc. Lond.* B **283**, 452–457.
Mims, W. B. 1972 Envelope modulation in spin-echo experiments. *Phys. Rev.* B **5**, 2409–2419.
Pecoraro, V. L., Baldwin, M. J., Caudle, M. T., Hsieh, W. & Law, N. A. 1998 A proposal for water oxidation in photosystem II. *Pure Appl. Chem.* **70**, 925–929.
Peloquin, J. M., Campbell, K. A., Randall, D. W., Evanchik, M. A., Pecoraro, V. L., Armstrong, W. H. & Britt, R. D. 2000 ^{55}Mn ENDOR of the S_2-state multiline EPR signal of photosystem II: implications on the structure of the tetranuclear Mn cluster. *J. Am. Chem. Soc.* **122**, 10 926–10 942.
Randall, D. W., Gelasco, A., Caudle, M. Y., Pecoraro, V. L. & Britt, R. D. 1997 ESE–ENDOR and ESEEM characterization of water and methanol ligation to a dinuclear Mn(III)Mn(IV) complex. *J. Am. Chem. Soc.* **119**, 4481–4491.
Tang, X. S., Sivaraja, M. & Dismukes, G. C. 1993 Protein and substrate coordination to the manganese cluster in the photosynthetic water oxidizing complex: ^{15}N and ^{1}H ENDOR spectroscopy of the S_2 state multiline signal in the thermophilic cyanobacterium *Synechococcus elongatus*. *J. Am. Chem. Soc.* **115**, 2382–2389.
Vrettos, J. S., Limburg, J. & Brudvig, G. W. 2001 Mechanism of photosynthetic water oxidation: combining biophysical studies of photosystem II with inorganic model chemistry. *Biochim. Biophys. Acta* **1503**, 229–245.
Yachandra, V. K., Sauer, K. & Klein, M. P. 1996 Manganese cluster in photosynthesis: where plants oxidize water to dioxygen. *Chem. Rev.* **96**, 2927–2950.
Zimmermann, J. L. & Rutherford, A. W. 1984 EPR studies of the oxygen-evolving enzyme of photosystem II. *Biochim. Biophys. Acta* **767**, 160–167.

Discussion

C. Zhang (*Department of Biochemistry, Lund University, Lund, Sweden*). If the alcohol binds to the Mn cluster and replaces water, why does it not affect oxygen evolution?

R. D. Britt. It is rather amazing, you can take the methanol concentration up to of the order of 30% and still get good O_2 evolution. I think the point is that in these ESEEM experiments we are probing the S_2 state, and the ligation can change by S_4 when O_2 is produced. There are two limiting cases: (i) by S_4, with additional Mn cluster oxidation, the equilibrium now favours water binding at the site where the alcohol binds at S_2; or (ii) alcohol and water are in fast exchange at this site, and the exchange rate exceeds *ca*. 1 kHz rate for O_2 production at S_4.

C. Dismukes (*Department of Chemistry, Princeton University, Princeton, NJ, USA*). Have you reconciled the model for water binding with the kinetics of water exchange measured by Tom Wydrzynski (*Photobioenergetics, Research School of Biological Sciences, The Australian National University, Canberra, Australia*) using mass spectrometry? He found a slow S_1 equivalent to one-hundredth of the water exchange rate for the S_2 state.

R. D. Britt. Professor Dismukes raises an important point, that spectroscopic measurements need to be carefully correlated with the mass spectrometry results. We are leaning towards a model where one substrate binds to the Mn cluster and another ligates to the proximal calcium. That would tend to predict that one site-specific comparison would show a stronger Mn oxidation state dependence than the other. To make the specific comparison of S_2 and S_1, we would need to be able to get ESEEM or ENDOR on the integer spin S_1 state, which we have not done to date.

P. Fromme (*Max-Volmer-Laboratorium für Chemie und Biochemie, Technische Universität, Berlin, Germany*). Methanol changes the properties of SO, inducing a multiline signal. Has anybody used EXAFS to investigate changes in the Mn–Ca and Mn–Mn distances upon alcohol binding?

R. D. Britt. Interesting question. I am not sure if a detailed EXAFS comparison of alcohol versus no alcohol has been done. Dr Yachandra would know.

G. W. Brudvig (*Department of Chemistry, Yale University, New Haven, CT, USA*). How many protons are associated with the water assigned as a ligand to calcium? Studies with deuterium gave a value of 2, but you have a hydroxide in your model.

R. D. Britt. I would say at this point that the ESEEM could accommodate either one or two. With the current simulations, if two, the second would have to be more

distant from the Mn cluster than the first, but there is no problem with that being the case.

M. W. C. Evans (*Department of Biology, University College London, London, UK*). Are your ENDOR spectra the same across their width, since you may be detecting sites other than Mn?

R. D. Britt. We have not seen such effects. We are careful to do good light–dark subtractions to null out other signals. At 4.2 K or higher, we do not see interference from the Fe–Q_A signal because it has a very short phase memory (T_2).

GLOSSARY

CW: continuous wave
ENDOR: electron nuclear double resonance
EPR: electron paramagnetic resonance
ESE: electron spin echo
ESEEM: electron spin echo envelope modulation
OEC: oxygen-evolving complex
PSII: photosystem II
RF: radiofrequency